Segmentation of X-ray Images by 3D-2D Registration based on Multibody Physics

Jérôme Schmid and Christophe Chênes

Geneva School of Health, University of Applied Sciences of Western Switzerland

Abstract. X-ray imaging is commonly used in clinical routine. In radiotherapy, spatial information is extracted from X-ray images to correctly position patients before treatment. Similarly, orthopedic surgeons assess the positioning and migration of implants after Total Hip Replacement (THR) with X-ray images. However, the projective nature of X-ray imaging hinders the reliable extraction of rigid structures in X-ray images, such as bones or metallic components. We developed an approach based on multibody physics that simultaneously registers multiple 3D shapes with one or more 2D X-ray images. Considered as physical bodies, shapes are driven by image forces, which exploit image gradient, and constraints, which enforce spatial dependencies between shapes. Our method was tested on post-operative radiographs of THR and thoroughly validated with gold standard datasets. The final target registration error was in average 0.3 ± 0.16 mm and the capture range improved more than 40% with respect to reference registration methods.

1 Introduction

The registration of pre-interventional 3D data to X-ray images is a challenging task due to the projective nature of the X-ray modality. Here, we address the registration problem by deriving 3D shapes from 3D data and by registering them to X-ray images. We express the shape registration as the evolution of shapes in a multibody physics framework – where shapes are driven by forces based on image information and by constraints to enforce spatial coherence.

X-ray imaging has many advantages such as availability, affordability and relatively low doses. These factors have favored its integration in clinical computer-assisted applications such as radiotherapy [1], interventional radiology [2] and orthopedic surgery [3–6]. In these applications, a single or multiple X-ray images are processed to extract spatial information to prepare or guide an intervention, or to analyze post-operative results.

But X-ray images are difficult to process since their projective nature is associated with loss of image information, overlapping of structures and perspective deformations. Many applications rely on 3D-2D registration methods [7] to tackle this issue.

In 3D-2D registration methods, a pre-interventional 3D dataset is registered with intra-interventional [1, 3] or post-interventional [6] 2D X-ray images – by optimizing the shape, position and orientation of the 3D dataset. The nature

of the 3D dataset varies, it can be for instance a 3D shape (e.g., derived from statistical shape models [5, 6] or CAD modeling [8]). Or a volumetric image such as Computed Tomography (CT) [9, 4, 10] or Magnetic Resonance (MR) [11, 4, 12].

Most approaches are based on Digitally Reconstructed Radiographs (DRR) [1, 2, 9, 10, 13], which are virtual radiographs created from volumetric images, commonly CT volumes. DRR-based registration methods find the optimal shape or transformation parameters that maximize a similarity metric between the computed DRRs and the corresponding X-ray images.

DRR-based approaches provide accurate results but have low capture ranges [7] due to their sensitivity to local optima in the objective function. Therefore, alternative strategies were imagined to avoid using DRR by directly exploiting gradients of the volumetric and X-ray images. Approaches are mainly classified based on the space in which gradients are compared [7], i.e., the X-ray [14, 15] or the 3D data [4, 3, 12] space.

The registration of 3D data to a single X-ray image often results in "out-of-plane" errors occurring in the source to detector direction. For example, when 3D shapes are registered to a single X-ray image the registered shapes can present incorrect spatial adjacency – despite low image projection errors. This issue particularly affects the estimation of implant orientation [6] or joint kinematics [8].

We target the rigid 3D-2D registration of shapes derived from 3D data to one or several X-ray images. Shape registration is equivalent to finding the best transformation (position and orientation) that correctly projects the shape onto the X-ray images. Most shape-based approaches depend on the extraction of the shape silhouettes in the X-ray images – a segmentation task difficult to automate, time-consuming when performed manually and whose accuracy impacts the registration outcome [7, 16].

Our work is original in computing the optimal transformation of shapes by considering the shapes as bodies evolving in a multibody physics framework. Multibody physics systems simulate the evolution of several bodies according to modeled Newtonian laws of motion. Rigid body motion is driven by user-defined external forces and subject to damping and inter-bodies constraints.

In [17], a similar approach was presented in which external forces were based on the minimization of distance between projected shape contours and extracted silhouettes from X-ray images. Our work avoids X-ray segmentation by using forces based on the similarity between DRRs and X-ray images. Despite the use of DRRs, our force-based method leads to large capture ranges by using an image similarity computation based on block matching.

Our approach is particularly novel in applying constraints between shapes to improve the simultaneous registration of multiple shapes. Constraints avoid non-plausible shape configuration such as inter-penetrations and provide robustness against out-of-plane errors. We demonstrate the good performances of our approach with publicly available gold standard datasets and preliminary data in the context of Total Hip Replacement (THR).
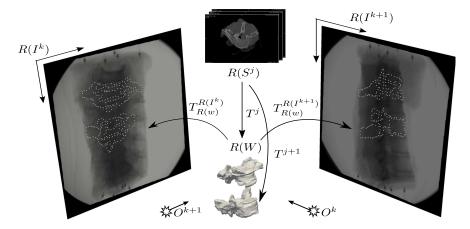
2   3D-2D Registration

Our approach targets the rigid 3D-2D registration of pre-interventional 3D data to one or several X-ray images. The 3D data can be composed of 3D models (e.g., CAD models of implants) or volumetric medical images – hereafter referred to as volumes to differentiate them from X-ray images. We derive 3D shapes from the pre-interventional 3D data, the registration problem is thus equivalent to registering the 3D shapes to the X-ray images.

2.1   Geometry and Shape Preparation

The geometry involved in our approach is depicted in Fig. 1. N X-ray images I^k ($k \in [1, N]$) are expressed in their local coordinate system (CS) $R(I^k)$ and are positioned with respect to a common world CS $R(W)$ based on rigid transformations $T_{R(W)}^{R(I^k)}$. We assume that the X-ray imaging system is calibrated – i.e., transformations and projective characteristics of X-ray images I^k (position of X-ray source O^k, pixel size) are known.

M shapes S^j ($j \in [1, M]$) are represented as triangular meshes and are expressed in their local CS $R(S^j)$. Each shape S^j is registered to the X-ray images I^k by optimizing the rigid transforms $T_{R(S^j)}^{R(W)} = T^j$ so that each shape is correctly projected onto the corresponding X-ray images. Shapes S^j are derived from the 3D pre-interventional data: CAD models are straightforwardly converted to triangular meshes, while volumes V^j are segmented to produce shapes after reconstruction.

Fig. 1. Illustration of the 3D-2D registration with X-ray images from [3]. Shapes S^j and S^{j+1} share a same CS $R(S^j)$ as they were reconstructed from the same CT volume $V^j(= V^{j+1})$. The registration jointly optimizes the rigid transformations T^j and T^{j+1} so that shapes positioned in the world CS are correctly projected on images I^k and I^{k+1}.

2.2   Method Overview

Our 3D-2D registration starts with a Force-Based (FB) registration (Sect. 3), which repeats for each shape 3 major steps until convergence (Fig. 2): (i) point computation (Sect. 3.1), (ii) force calculation (Sect. 3.2) and (iii) shape position update (Sect. 3.3). After the FB registration, a registration based on gradient correlation, denoted as GCB, is applied to refine the results (Sect. 4). The overall process "FB followed by GCB" will be referred to as the Enhanced Force-Based method (EFB).
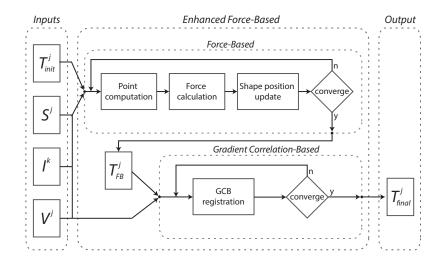

Fig. 2. Overview of our 3D-2D registration method: Enhanced Force-Based; Inputs: initial transformations for each shape (T_{init}^j), the shapes (S^j), the X-ray images (I^k) and the volumes (V^j); Intermediate output: FB result transformation T_{FB}^j; Output: final transformation T_{final}^j

3   Force-Based Registration

3.1   Point Computation

Based on the current transformation T^j of the shape S^j and an X-ray image I^k with corresponding projective properties, the associated volume V^j is used to generate a DRR D^{jk}. Since we use a ray-casting approach [9] to generate the DRR, we restrict our method to X-ray based modalities (e.g., 3D Rotational X-ray Imaging or CT). For shapes not derived from medical volumes, we create artificial volumes by rasterizing the shapes into binary images and we apply the same DRR generation approach (Fig. 3a).
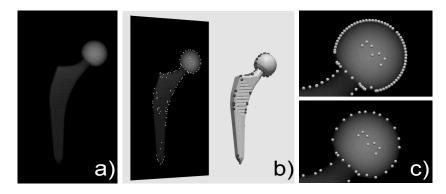
Fig. 3. DRR example and point selection. **a)** DRR generated from an artificial volume of an implant model. **b)** A silhouette criterion selects a subset of shape vertices (dark spheres) so that projected points (bright spheres) on the DRR image lie on strong edges. **c)** The number of projected points is reduced by keeping a single point within image blocks.
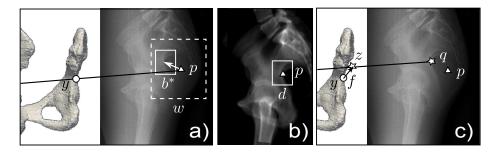
Vertices of the shape S^j are then filtered with a *silhouette criterion* such as in [5]. This criterion keeps vertices belonging to edges with front and back facing triangles with respect to a viewpoint located at the X-ray source position O^k (Fig. 3b). We chose the silhouette procedure to select points of interest that will exhibit a significant local gradient variation in the projected image.

The selected subset of vertices is then projected onto the image (Fig. 3b). We divide the image into a grid with blocks of $G \times G$ pixels and reduce all points falling into a block to a single point by choosing the closest point to the block point barycenter (Fig. 3c). This reduction process results in projected points p_i^{jk} corresponding to *source* shape vertices y_i^{jk} ($i \in [1, L^{jk}]$).

For each projected point p_i^{jk} defined in DRR image D^{jk} we look for a position in the corresponding X-Ray image I^k which maximizes a local similarity criterion. A block d_i^{jk} of $B \times B$ pixels is defined around each projected point p_i^{jk} in D^{jk} (Fig. 4b). Similarly, we specify a search window w_i^{jk} of $W \times W$ pixels for each projected point in I^k (Fig. 4a).

A block matching procedure is subsequently applied by finding the block b_i^{*jk} within the search window that matches at best each block d_i^{jk} (Fig. 4a). *Target* projected points q_i^{jk} are chosen as the center positions of the resulting blocks b_i^{*jk}. The block matching technique increases the capture range of registrations method [18] and speeds up the DRR computation since we can restrict its computation within the blocks only.

We chose the Gradient Correlation (GC) [9] for the similarity metric due to its good performance in DRR-based 3D-2D registration [10, 13]. $GC(b, d)$ maximizes the alignment of gradient vectors in blocks b and d normalized by the mean gradient vector of the corresponding block. A gradient-based metric is adequate to capture the gradient variations near the projected silhouette points.

Fig. 4. Force-based registration. **a)** A silhouette shape point y ($\bullet$) is projected on p ($\triangle$) in the X-ray image I and **b)** on the DRR D. In I, a block b^* is found within a search window w such that it matches best the block d in D. **c)** Based on the ray (O, q), where O is the position of the X-ray source and q ($\star$) is the center of b^*, a new shape point z ($\star$) is computed to produce the image force f.

3.2   Force Calculation

The optimization of the transformations T^j is indirectly performed by controlling the motion of the shapes S^j that evolve in a system built upon Newtonian laws of motion. Each shape S^j is modeled as a rigid body with mass m^j driven by Newtonian dynamics and subjected to external forces and constraints, as well as damping γ.

We devise external forces to alter the position of shapes in the world CS so that transformations T^j are optimized. *Image* forces enforce at the point level the similarity between local areas of the DRRs and the X-Ray images. Given a source point y_i^{jk} of a shape S^j selected at the point selection stage, we compute a force f_i^{jk} at y_i^{jk} that follows the Hooke's law of a spring with stiffness l^j:

$$f_i^{jk} = l^j * (z_i^{jk} - y_i^{jk}) \tag{1}$$

where a target point z_i^{jk} is computed as the projection of y_i^{jk} on the ray passing through the X-ray source O^k and the target projected point q_i^{jk} resulting from the block matching (Fig. 4c). This force "attracts" the shape to a position where the image similarity is maximized – i.e., a location satisfying the 3D-2D registration problem. Given a shape S^j, forces calculated for each image I^k are back-transformed in the world CS and summed at vertex level – providing a natural way to consider multiple X-ray images:

$$f_i^j = \sum_{k=1}^{N} (T_{R(w)}^{R(I^k)})^{-1} f_i^{jk} \tag{2}$$

3.3   Shape Position Update

A simulation step of the physics system updates the position of the rigid bodies based on their current state (velocity, position), the external forces and the damping γ (which produces a resisting force with an amplitude proportional to body velocity). This is performed by a numerical integration scheme which solves a set of algebraic and differential equations. The resulting position of a shape S^j is eventually used to update the transformation T^j.

A simulation step also considers constraints that model dependencies between shapes. Examples of constraints are collision response to avoid colliding bodies and the modeling of joints with various degrees of freedom. For instance, a pivot constraint can be defined between two bodies to have them rotate around a relative rotation center.

The simulation runs until shape motion reaches an equilibrium – a state which balances respect of constraints and image similarity maximization. In practice, a perfect equilibrium is not always observed since joint constraints can be over restrictive yielding a small "oscillation" of the shape position around the equilibrium. This issue is addressed by "softening" the constraints to allow small violations, like an inter-penetration threshold between bodies or a small distance between pivot centers.

The equilibrium is also affected by the accuracy of the block matching. A sub-pixel accuracy cannot be reached with block matching since the computation of block positions is restricted to integer pixel locations. Consequently, image forces at some vertices can contribute to the position instability around the equilibrium.

The variation of shapes could be analyzed between two successive steps to stop the simulation when the Euclidean distance between the shape vertices is below a threshold. However, choosing an adequate threshold value is not an easy task since e.g. a too big value can lead to premature termination. An alternative approach is to run the simulation for a fixed number of steps n – such value being selected based on experiments.

4   Enhanced Force-based Registration by Gradient Correlation Refinement

After completion of the force-based registration FB, the GCB refinement is performed to improve the accuracy of our block-based approach. This refined registration does not rely anymore on the physics system but instead it optimizes the transformation T^j of a shape S^j by maximizing the sum of the GC similarities between the DRRs D^{jk} and X-ray images I^k [10]. Similarly to the block matching process, we only compute the sum of similarities Φ^j inside blocks d_i^{jk}:

$$\Phi^j = \sum_{k=1}^{N} \sum_{i=1}^{L^{jk}} GC(b_i^{jk}, d_i^{jk}) \tag{3}$$

where blocks b_i^{jk} and d_i^{jk} are computed for the X-ray image I^k and the DRR D^{jk}, and are centered on the filtered projected points p_i^{jk} with the same selection procedure of the FB method (Sect. 3.1).

As suggested by [10], we used a Powell-Brent optimizer for which we automatically compute the parameter scales. For an average translation step of t mm, we choose an angular step α such as $tan(\alpha) = t/r$, where r is the radius of the enclosing sphere of the shape. Isotropic translation and rotation scales are finally set to $1/t$ and $1/\alpha$. The rotation center of the rigid transformation T^j is set to the gravity center of the shape S^j.

The rationale behind using the GCB is that after FB we are close to the final solution so that constraints are not necessary at this stage. A way to consider constraints in Eq. 3 would depend on the type of constraints. For instance, we could add a penalty term to minimize the distance between pivot centers for pivot constraints.

5   Experiments

We tested our FB and EFB methods with two experiments. The first experiment uses gold standard 3D-2D registration datasets and exemplifies the use of multiple X-ray images. In the second experiment, we registered multiple shapes to a single post-THR X-ray image.

Multibody physics were implemented with Bullet Physics library[1], while block-matching and image similarity optimization were implemented with ITK[2]. We used a computer with i7 core and 6GB RAM running Windows 7. Table 1 reports the values of the different parameters.

Table 1. Experiment parameters for the FB first and second passes, and for the GCB refinement.

Parameters			FB first pass	FB second pass	GCB
block size	B	(Sect. 3.1, 4)	15 px	11 px	9 px
window size	W	(Sect. 3.1)	20 px	10 px	-
reduction block size	G	(Sect. 3.1)	10 px	10 px	10 px
mass	m^j	(Sect. 3.2)	1 kg	1 kg	-
stiffness	l^j	(Sect. 3.2)	0.2 N.m^{-1}	0.2 N.m^{-1}	-
damping	γ	(Sect. 3.3)	0.99 N.s.m^{-1}	0.99 N.s.m^{-1}	-
# steps	n	(Sect. 3.3)	40	40	-
translation step	t	(Sect. 4)	-	-	1 mm

We applied a multi-resolution strategy with two consecutive passes in the FB method. In the first pass, the sizes of the search window W and block B were

---

[1] http://www.bulletphysics.org

[2] http://www.itk.org

chosen to ensure large capture ranges and improve robustness against image artifacts. In the second pass, the sizes were reduced to improve accuracy and speed.

Same physical parameters were set for all shapes. We experimentally defined a number of 40 simulation steps per pass – the value being an upper limit as sometimes we observed earlier convergence to a stable equilibrium. The values of the image parameters B, G and W were chosen for an average pixel size of 0.5 mm and for standard clinical usage of X-ray imaging (e.g., average source to detector distance of 1200 mm).

5.1   Validation on Gold Standard Datasets

We used two gold standard datasets *Dataset A* [3] and *Dataset B* [4], which contain CT images with 8 and 5 human vertebrae. Datasets include calibrated X-ray images registered to a world CS. For each vertebra, a gold standard transformation from the CT CS to the world CS is provided.

Corresponding works [3, 4] describe tests for objective evaluation, which include pairs of quasi-perpendicular X-ray images, starting positions and reference points to compute mean Target Registration Error (mTRE) [3]. We used the same testing conditions and data except for the size of X-ray images in *Dataset B* which was divided by 2 to speed-up DRR generation and satisfy block parameters reported in Table 1. Additionally, we coarsely reconstructed the shapes of vertebrae from CT volumes.

We ran a total of 3850 (1600 on *Dataset A* and 2250 on *Dataset B*) tests to validate our methods – with a test taking about 5 minutes to complete. A single vertebra was optimized during a test, hence constraints were not necessary. Our FB and EFB methods were compared against the following approaches: Intensity-Based (IB) [9], Gradient-Based (GB) [4], Reconstruction-Based (RB) [11] and Robust Gradient Reconstruction-Based extension (RGRBe) [12].

The accuracy of registration was assessed with the mTRE. Success criteria was set to $mTRE \leq 2\,mm$ and Capture Range (CR) was defined as the distance from the reference position for which 95% of the registrations were successful [12]. Success Rate (SR) was defined as the percentage of successful tests.

Table 2 reports the results of compared methods for both datasets. For *Dataset A* figures were copied from [12]. For *Dataset B* data was only available for the GB method, from which we computed the metrics.

The performances of the FB method were satisfactory. The CR was almost as good as the reference method RGRBe on *Dataset A* (10.3 vs. 11 mm) and larger than GB on *Dataset B*. However, FB was less accurate than RGRBe on *Dataset A* (0.65 vs. 0.32) and *GB* on *Dataset B* (0.77 vs. 0.32). SR was in average greater than 70%.

The use of GCB improved the results of the FB method for both datasets (e.g., Fig. 5 for *Dataset A*) – with improvements in CR and SR values and a significant difference in accuracy (p-value<1e-16, Wilcoxon matched pairs test). We tested a direct application of the GCB on *Dataset A* which produced poor

Table 2. Comparison of our 3D-2D registration methods Force-Based (FB) and Enhanced Force-Based (EFB) with existing methods: Intensity-Based (IB) [9], Gradient-Based (GB) [4], Reconstruction-Based (RB) [11] and Robust Gradient Reconstruction-Based extension (RGRBe) [12]; A = Accuracy (mm), CR = Capture Range (mm) and SR = Success Rate (%)

	Dataset A						*Dataset B*		
	IB	GB	RB	RGRBe	**FB**	**EFB**	GB	**FB**	**EFB**
A	0.65	0.38	0.43	0.32	**0.65**	**0.22**	0.32	**0.77**	**0.39**
CR	3.00	6.00	5.00	11.00	**10.30**	**15.70**	4.20	**6.40**	**7.40**
SR	-	56.00	65.00	92.00	**73.20**	**80.00**	51.40	**71.90**	**74.10**

results (accuracy of 0.6 mm, SR of 21.6%). This upholds the use of our EFB method which combines the force-based method with the GCB method.

With our EFB method, we measured a CR 42% higher than the reference method on *Dataset A* with an improvement in accuracy (0.22 vs. 0.32 mm). Though our SR (80%) was below RGRBe (92%), the greater CR of the EFB method (15.7 mm) compared to RGRBe (11 mm) highlighted the better consistency of our method.

The EFB approach also yielded better results on *Dataset B*. CR and SR were improved by 76% and 44%. Accuracy significantly decreased (p-value<0.0001) to a low value of 0.39 mm but it remained greater than the accuracy of GC method (p-value<0.0001).
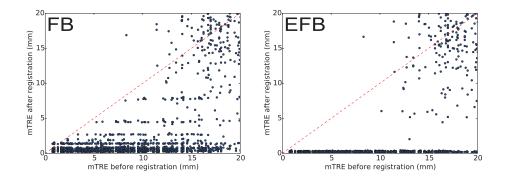

Fig. 5. Registration results on *Dataset A* for FB and EFB methods.

5.2   Experiment on Total Hip Replacement Data

We tested our EFB method on THR post-operative data by registering shapes of hip implants and hip bone to a single anteroposterior (AP) X-ray image.

This experiment investigates the use of our 3D-2D registration to compute the anteversion (RA) and inclination (RI) angles. These angles quantify the cup orientation with respect to the hip bone and are essential for evaluation of outcome after THR [6].

After ethical approval, we acquired post-operative CT images and AP radiographs from 3 patients who underwent THR. The manufacturer provided the shapes of implants which we carefully registered to the CT volumes, while the hip bone was manually segmented in the CT dataset. Based on the reconstructed hip, we computed the RA and RI angles according to the radiographic convention [19].

A hip implant is composed of two parts which are mechanically linked by a pivot joint. The femoral implant is made of the stem and head while the acetabular implant includes the cup and the liner. For each part, we created a shape derived from the implant CAD models of the manufacturer.

We conducted an experiment to register the implants and hip bone to the AP radiograph – by keeping the same parameters as in previous experiment (Table 1). To remove the bias of using the post-operative CT volume with implants, we built for each implant shape an artificial binary volume with isotropic spacing of 0.5 mm (Sect. 3.1). Similarly, shapes were not initialized from the configuration of the post-operative CT, but were instead initialized based on manually placed landmarks.

We modeled pivot constraints between the femoral and acetabular shapes by using the rotation center provided by the manufacturer and defined in the CS of each shape. An additional pivot constraint was defined between the hip bone and the acetabular implant. The pivot center of the hip bone was estimated as the center of the sphere, with same radius as the cup, which fitted at best the acetabulum area of the bone.

To account for inaccuracies in estimating the pivot centers, we relaxed constraints by allowing slight deviations from constrained states. We used the Error Reduction Parameter (ERP) of Bullet library – where an ERP value$<$1 softens the joint, while a value of 1 yields a perfect joint. We chose an ERP value of 0.8.

Pixel size and source-to-detector distance of X-ray images were known. But compared to the previous experiment a gold-standard transformation from CT to X-ray CS was not available. Thus, we assessed the relative positioning of the cup with respect to the hip bone.

We measured a Surface Distance error [20] (SD in mm) between acetabular implants in CT and X-ray images. We also computed Absolute Differences (AD in °) between expected (CT) and computed (X-ray) RA and RI angles. Results for FB and EFB methods are reported in Table 3.

When using constraints we observed a good projection of shapes after registration (e.g., Fig. 6c) and measured an average SD of 0.61 ± 0.59 mm – despite an approximate initialization (e.g., Fig. 6a). The AD was low for the RA ($0.57 \pm 0.50°$) but was high for the RI – due to a large AD of 5° computed for one patient. By removing this patient's data, the AD improved about 50% for both angles.

Table 3. Results of our Enhanced Force-Based method (EFB) on THR data with and without the use of constraints; Measures are the Absolute Differences (AD) for the anteversion (RA) and inclination (RI) angles, and the Surface Distance error (SD).

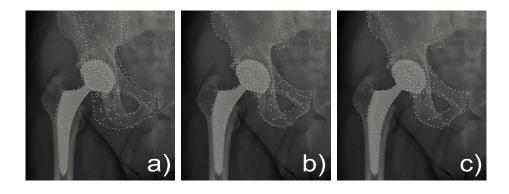|	AD RA	AD RI	SD
EFB with pivot constraints	$0.57 \pm 0.50°$	$2.37 \pm 2.29°$	0.61 ± 0.59 mm
EFB without pivot constraints	$3.95 \pm 4.96°$	$9.09 \pm 8.04°$	2.03 ± 2.05 mm

Fig. 6. Example of projected points onto X-ray images for one patient. **a)** The initialization is approximate but the points appear well projected in the final results **b)** without and **c)** with the use of pivot constraints.

When constraints were not used, we measured a large increase of the distance and angle errors (e.g., 0.57 to 3.95 for the AD of RA). We observed out-of-plane errors illustrated in Fig. 7b in which the cup left the acetabular socket in the detector-to-source direction – despite a good projection of points on the X-ray image (Fig. 6b).

Despite a low number of subjects in this experiment, results were very promising. They highlighted the EFB strong potential to accurately segment multiple shapes from a single X-ray image.

6   Discussion and Conclusion

Based on Markelj et al.'s classification [7], we devised a novel hybrid approach mixing projection (block-matching coupled with DRR) and back-projection (force driven optimization) techniques. Our approach relies on a multibody physics system that provides a natural and efficient way to tackle the simultaneous registration of several shapes with multiple X-ray images.

Compared to other existing methods, our approach generally returned more accurate results with a larger capture range in gold standard benchmarks using two radiographs. In particular, the block-based matching improved the capture
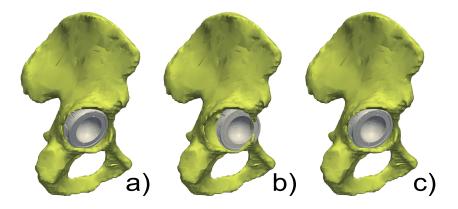
Fig. 7. Illustration of the performances in using constraints for one patient. The positioning of the acetabular implant looks quite similar between the **a)** expected and **c)** the result with constraints. **b)** Without constraints, the acetabular implant is clearly in the wrong location.

range compared to direct DRR-based approaches. Physical constraints brought robustness to the registration of multiple shapes to a single X-ray image, but additional testing is necessary to assess its viability in clinical use (e.g., cup orientation computation [6] or joint tracking by fluoroscopy [8]).

A limitation of our approach is the need of shapes of the patient, which may require some 3D segmentation. However, we observed that our approach was not very sensitive to the segmentation quality, which is not the case for techniques based on 2D X-ray segmentations [16]. Nevertheless, current work focuses on creating forces based on statistical shape models, like [21], to remove this dependency of patient-specific shapes as in [5, 6].

Similarly, we plan to avoid the use of invasive CT scans by adding new image forces which do not require DRR and support MR images. It could be based on the back projected gradients [12]. By adding new forces, we can easily extend our framework while preserving its advantages such as constraints.

References

1. Fu, D., Kuduvalli, G.: A fast, accurate, and automatic 2D–3D image registration for image-guided cranial radiosurgery. Med Phys **35** (2008) 2180–2194
2. Hurvitz, A., Joskowicz, L.: Registration of a CT-like atlas to fluoroscopic X-ray images using intensity correspondences. IJCARS **3** (2008) 493–504

3. van de Kraats, E., Penney, G., Tomazevic, D., van Walsum, T., Niessen, W.: Standardized evaluation methodology for 2-D-3-D registration. IEEE Trans Med Imag **24** (2005) 1177–1189

4. Tomazevic, D., Likar, B., Slivnik, T., Pernus, F.: 3-D/2-D registration of CT and MR to X-ray images. IEEE Trans Med Imag **22** (2003) 1407–1416

5. Benameur, S., Mignotte, M., Parent, S., Labelle, H., Skalli, W., de Guise, J.: 3D/2D registration and segmentation of scoliotic vertebrae using statistical models. Comput Med Imag Graph **27** (2003) 321–337

6. Zheng, G., von Recum, J., Nolte, L.P., Grützner, P.A., Steppacher, S.D., Franke, J.: Validation of a statistical shape model-based 2D/3D reconstruction method for determination of cup orientation after THA. IJCARS **7** (2012) 225–231

7. Markelj, P., Tomazevic, D., Likar, B., Pernus, F.: A review of 3D/2D registration methods for image-guided interventions. Med Image Anal **16** (2010) 642–661

8. Koyanagi, J., Sakai, T., Yamazaki, T., Watanabe, T., Akiyama, K., Sugano, N., Yoshikawa, H., Sugamoto, K.: In vivo kinematic analysis of squatting after total hip arthroplasty. Clin Biomech **26** (2011) 477–483

9. Penney, G., Weese, J., Little, J., Desmedt, P., Hill, D.L.G., Hawkes, D.: A comparison of similarity measures for use in 2-D-3-D medical image registration. IEEE Trans Med Imag **17** (1998) 586–595

10. van der Bom, I., Klein, S., Staring, M., Homan, R., Bartels, L., Pluim, J.: Evaluation of optimization methods for intensity-based 2D-3D registration in x-ray guided interventions. In: Proc. SPIE 7962, Medical Imaging. (2011) 796223–796238

11. Tomazevic, D., Likar, B., Pernus, F.: 3-D/2-D registration by integrating 2-D information in 3-D. IEEE Trans Med Imag **25** (2006) 17–27

12. Markelj, P., Tomazevic, D., Pernus, F., Likar, B.: Robust gradient-based 3-D/2-D registration of CT and MR to X-Ray images. IEEE Trans Med Imag **27** (2008) 1704–1714

13. Kubias, A., Deinzer, F., Feldmann, T., Paulus, D., Schreiber, B., Brunner, T.: 2D/3D image registration on the GPU. Pattern Recogn Image Anal **18** (2008) 381–389

14. Livyatan, H., Yaniv, Z., Joskowicz, L.: Gradient-based 2-D/3-D rigid registration of fluoroscopic X-ray to CT. IEEE Trans Med Imag **22** (2003) 1395–1406

15. Wein, W., Roeper, B., Navab, N.: 2D/3D registration based on volume gradients. In: Proc. SPIE. Volume 5747. (2005) 144–150

16. Mahfouz, M.R., Hoff, W.A., Komistek, R.D., Dennis, D.A.: Effect of segmentation errors on 3D-to-2D registration of implant models in X-ray images. J biomech **38** (2005) 229–239

17. Kurazume, R., Nakamura, K., Okada, T., Sato, Y., Sugano, N., Koyama, T., Iwashita, Y., Hasegawa, T.: 3D reconstruction of a femoral shape using a parametric model and two 2D fluoroscopic images. Comput Vis Image Understand **113** (2009) 202–211

18. Ourselin, S., Roche, A., Prima, S., Ayache, N.: Block matching: A general framework to improve robustness of rigid registration of medical images. In: Proc. MICCAI, Springer (2000) 557–566

19. Murray, D.: The definition and measurement of acetabular orientation. J Bone Joint Surg **75** (1993) 228–232

20. Roy, M., Foufou, S., Truchetet, F.: Mesh comparison using attribute deviation metric. Int J Image Graph **4** (2004) 127–140

21. Schmid, J., Magnenat-Thalmann, N.: MRI bone segmentation using deformable models and shape priors. In: Proc. MICCAI, Springer (2008) 119–126